

# A $2.5\ \mu\text{W}$ $30\ \text{nV}/\sqrt{\text{Hz}}$ Instrumentation Amplifier for Bioimpedance Sensors with Source Degenerated Current Mirror and DTMOS Transistor

Yu Xue, *Student Member, IEEE*, Kwantae Kim, *Senior Member, IEEE*,

**Abstract**—This paper proposes a low-power and low-noise instrumentation amplifier (IA) tailored for bioimpedance sensing applications. The design originates from a gain-boosted flipped voltage follower (FVF) transconductance (TC) stage and integrates two complementary circuit techniques to improve the noise performance. To achieve an optimal balance between input-referred noise and available voltage headroom, a source-degenerated current mirror (SDCM) is adopted, resulting in reducing the input-referred noise by 7.95% compared with a conventional current mirror structure. In addition, a dynamic threshold MOSFET (DTMOS) scheme is employed to enhance the effective transconductance, leading to a further 11.66% reduction in input-referred noise. Simulated in a 28 nm CMOS process demonstrate that the proposed IA achieves an input-referred noise floor of  $30\ \text{nV}/\sqrt{\text{Hz}}$  and a bandwidth of 1.44 MHz, while consuming only  $2.5\ \mu\text{W}$  from a 0.8 V supply. Compared to the baseline design, the proposed approach achieves a 32.4% reduction in power consumption without degrading noise performance. The complete design parameters are open-sourced in this paper, to ensure reproducibility and facilitate future developments.

**Index Terms**—Bioimpedance (BioZ), drain regulation amplifier, dynamic threshold MOS (DTMOS), flipped voltage follower (FVF), gain boosting cascode, input referred noise, loop gain, source degenerated current mirror (SDCM).

## I. INTRODUCTION

BIOIMPEDANCE (BioZ) sensing has emerged as a key modality for physiological monitoring, leveraging the frequency-dependent properties of biological tissues for real-time vital sign estimation. Applications span clinical and consumer domains, including heart rate [1], respiration [2], glucose monitoring [3], [4], hand gesture recognition [5], and early cancer detection [6]. Compact wearable [1], [7] and implantable [3] devices impose demand high-fidelity bioimpedance (BioZ) under tight power budgets, making low-power analog front-end essential due to miniaturization of battery-operated devices. This has driven extensive research into analog front-ends [1], [2], [7]–[12], where instrumentation amplifiers (IAs) are key to low-noise signal readout. Advances in low-noise design are critical to meet the resolution and energy demands of wearable and implantable BioZ systems.

Fig. 1 illustrates a typical voltage-readout front-end architecture in a BioZ sensor integrated circuit (IC), incorporating

This work was supported in part by the Aalto SemiSummer2025 Training Program granted by Aalto University School of Electrical Engineering and funded by the Finnish Semiconductor Industry.

The authors are with the Department of Electronics and Nanoengineering, School of Electrical Engineering, Aalto University, 02150 Espoo, Finland.

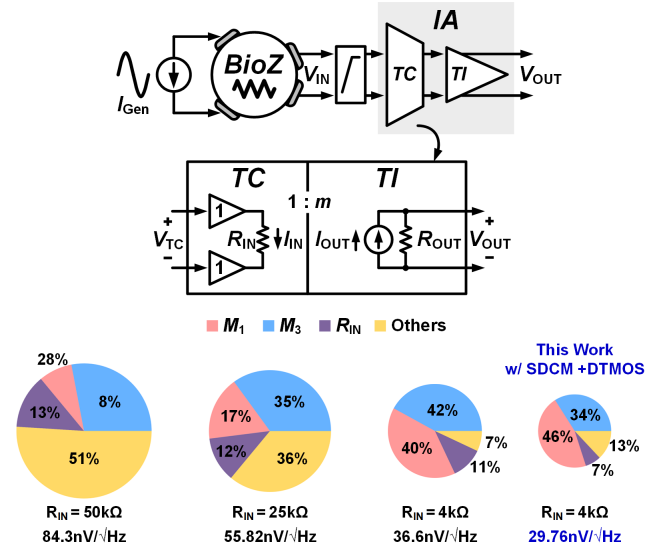


Fig. 1. Typical architecture of an IA in BioZ voltage readout [8]–[11] and the proposed IA and their noise breakdown at 100 kHz when simulated in 28 nm CMOS process.  $M_1$  and  $M_3$  can be found in Fig. 2.

an IA for signal amplification with minimized input-referred noise to detect subtle physiological variations [1], [6]–[12]. The IA comprises transconductance (TC) and transimpedance (TI) stages, where its gain is  $mR_{\text{OUT}}/R_{\text{IN}}$  [10], enabling precise voltage gain by resistance ratio. The TC stage is the front-end of the readout chain, employing a flipped voltage follower (FVF)-based buffer which is critical to overall noise, bandwidth, power consumption, and linearity performance, thereby directly impacting the accuracy and robustness of the BioZ measurement. The subsequent TI stage converts the current signal of the TC stage into a differential voltage across  $R_{\text{OUT}}$ .

Prior works [8]–[10], [12] have identified the input resistor  $R_{\text{IN}}$  as one of the primary contributors to the input-referred noise of IA. To achieve low noise performance, a small  $R_{\text{IN}}$  is preferred, while the associated loop gain degradation in the FVF circuit can be compensated by gain enhancement techniques. The input-referred thermal noise power spectral density (PSD) of the IA can be expressed as [14]:

$$\overline{v_{n,\text{IA}}^2} \approx \overline{v_{n,\text{M1}}^2} + \left( \overline{i_{n,\text{M3}}^2} + \overline{i_{n,R_{\text{IN}}/2}^2} \right) \left( \frac{R_{\text{IN}}}{2} \right)^2 = \frac{4kT\gamma}{g_{m1}} + \left( 4kT\gamma g_{m3} + 4kT \frac{R_{\text{IN}}}{2} \right) \left( \frac{R_{\text{IN}}}{2} \right)^2 \quad (1)$$

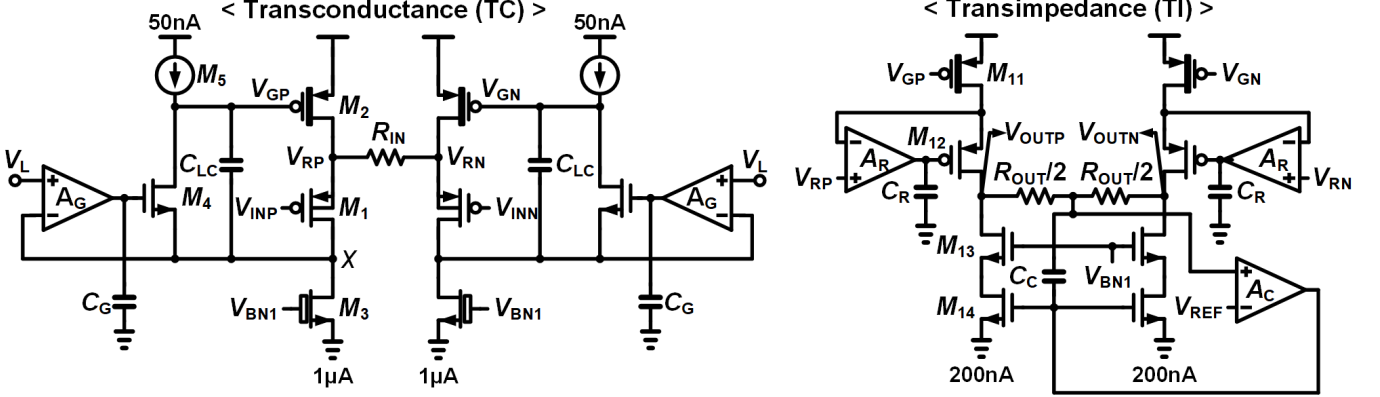


Fig. 2. Schematic of the baseline IA [9], [10], [13], [14].

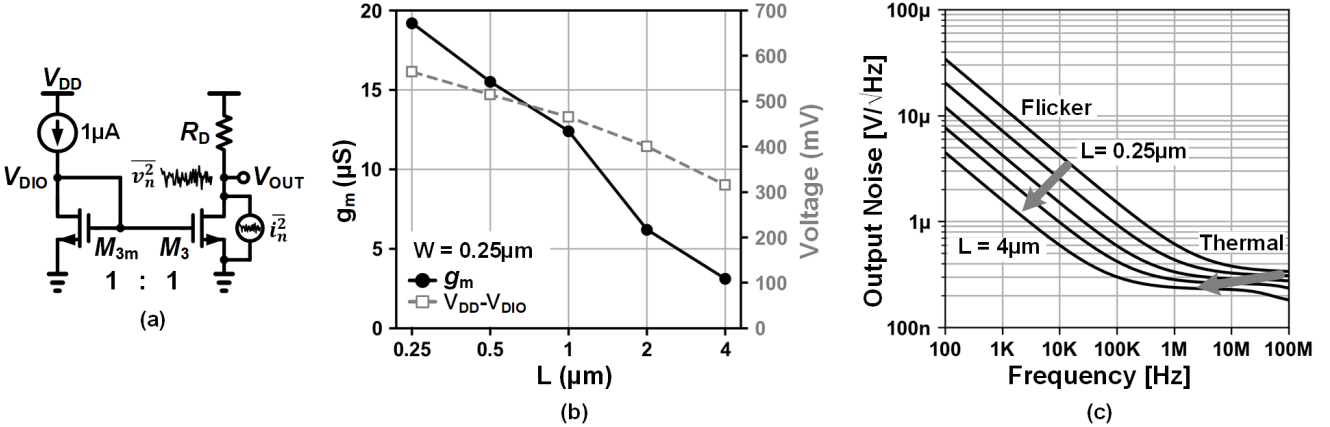


Fig. 3. (a) Schematic of a conventional current mirror, (b) simulated  $g_m$  and voltage headroom with different lengths, and (c) output noise spectral density versus frequency for different lengths.

where  $M_1$  and  $M_3$  denote the input transistor and the tail current source in the TC stage, respectively (Fig. 2),  $g_m$  is the transistor transconductance,  $k$  is the Boltzmann constant, and  $\gamma$  is the noise model parameter. As illustrated in Fig. 1, reducing  $R_{IN}$  from  $50\text{k}\Omega$  to  $4\text{k}\Omega$  significantly suppresses the input referred noise and make the noise contribution of  $R_{IN}$  to a negligible level. However, the noise contribution from  $M_3$  remain significant, accounting for approximately 42% of the total input-referred noise and forming a bottleneck to further improvement in noise performance.

Beyond noise performance, voltage headroom has also become a critical design aspect of analog circuits in advanced CMOS processes. As the supply voltage  $V_{DD}$  continues to scale down with technology, the available margin for signal swing and biasing is reduced [15]–[17]. This reduced headroom poses challenges for the design of IAs and is essential to address in parallel with noise reduction to ensure robust performance.

In this paper, we propose applying two noise reduction techniques to the IA for ultra-low-power BioZ sensor ICs: 1) a source degenerated current mirror (SDCM) and 2) a dynamic threshold MOS (DTMOS). The SDCM reduces noise from the tail current source  $M_3$ , with only a minimal penalty of 50 mV in the voltage headroom of the amplifier core ( $V_{DE}$  in Fig. 5). The DTMOS is employed to lower the noise

of the input transistor  $M_1$ , thereby further improving the noise performance of the IA. Notably, the two techniques are orthogonal and complementary, enabling their combined use to achieve improvements unattainable by either technique alone. Simulation results in a 28 nm CMOS process show that, when both schemes are applied together, the proposed IA achieves an 18.7% reduction in input-referred noise without any increase in power consumption compared to the baseline design. Under iso-noise conditions, the IA shows a 32.4% higher power efficiency.

This article is an extension of [18]. The remaining part of this article is organized as follows. Section II provides a comparative analysis and simulation results of two current mirrors, a conventional current mirror and a SDCM. Section III introduces the DTMOS scheme and its efficacy in enhancing the noise of the IA. Section IV presents the simulation results based on the proposed IA. Section V concludes this work and summarizes key contributions.

## II. NOISE ANALYSIS IN CURRENT MIRROR

As indicated by Eq. (1), reducing the total input-referred noise requires maximizing  $g_{m1}$  while minimizing  $g_{m3}$ . The

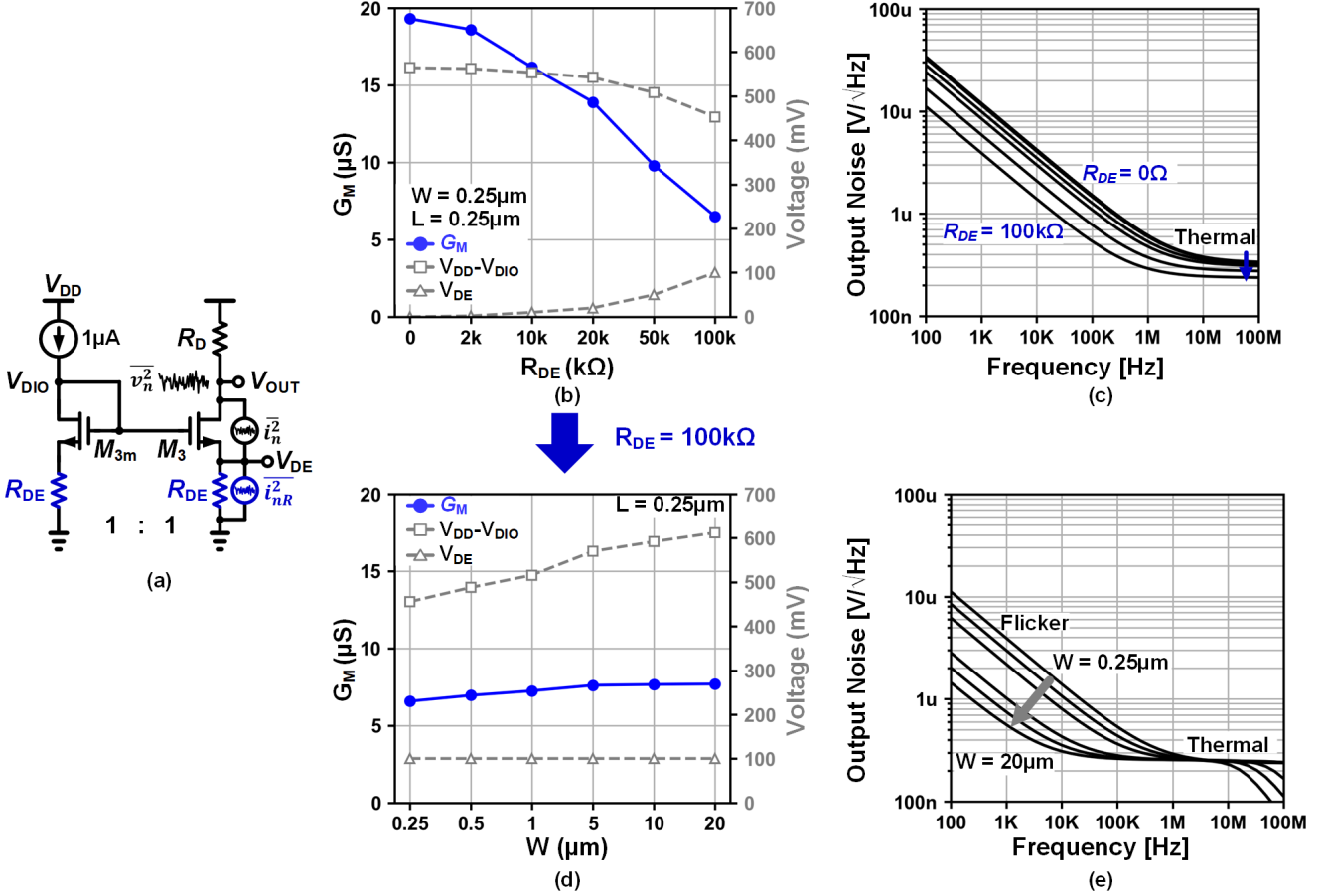


Fig. 4. (a) Schematic of a SDCM, (b) simulated  $G_m$  and voltage headroom versus  $R_{DE}$ , (c) output noise spectral density versus frequency for different  $R_{DE}$ , (d)  $G_m$  and voltage headroom versus width with a fixed  $R_{DE} = 100 \text{ k}\Omega$ , and (e) output noise spectral density versus frequency for different width.

term  $g_{m3}$ , corresponding to the current mirror transistor  $M_3$  in Fig. 2, contributes to the second term in Eq. (1).

#### A. Long Length Current Mirror

Fig. 3(a) illustrates a conventional current mirror, with transconductance  $g_m$  and the thermal noise PSD at the drain node given by

$$g_m = \frac{\partial I_D}{\partial V_{GS}} = \sqrt{\mu C_{\text{ox}} \frac{W}{L} I_D} = \frac{2 I_D}{V_{GS} - V_{TH}} \quad (2)$$

$$\overline{v_{n,CM}^2} = 4kT\gamma g_{m3} R_D^2 + \overline{v_{RD}^2}. \quad (3)$$

where  $\overline{v_{RD}^2}$  represents the noise PSD contributed by  $R_D$ . Here, we only consider the noise contributions from the mirrored branch,  $M_3$  and  $R_D$ , and exclude the noise from  $M_{3m}$ , as the IA is implemented in a differential architecture (Fig. 2). The first term in Eq. 3 reveals that the noise scales with  $g_{m3}$ . Under strong inversion and saturation, an increase in channel length leads to a lower  $g_m$ , which consequently reduces noise [10], [19]. However, a lower  $g_m$  demands a higher  $V_{GS}$ , increasing the drain voltage  $V_{DIO}$  and degrading the voltage headroom. This constraint becomes critical in advanced CMOS processes, where the supply voltage is limited to sub-1 V levels, as in the 28 nm CMOS process.

Fig. 3(b), (c) illustrate the trade-off between noise performance and voltage headroom by sweeping the length  $L$  of the current mirror device, while keeping the width  $W$  fixed at 250 nm, based on simulations in a 28 nm CMOS process. Since the maximum available channel length is limited to 1 μm in the used process, we adopted a series-stacking technique [20], where multiple identical transistors are connected in series so that the effective channel length equals the sum of the individual lengths. As  $L$  increases from 0.25 μm to 4 μm,  $g_m$  decreases from 18 μS to 3 μS, resulting in reduced output noise. However, the accompanying increase of  $V_{GS}$  significantly degrades the voltage headroom ( $V_{DD} - V_{DIO}$ ), resulting in a 220 mV drop from 550 mV to 310 mV (which is below half  $V_{DD}$ ). As a result, the limited headroom makes the conventional current mirror less favorable in low-supply IA design. This headroom problem becomes exacerbated as the CMOS process scales, since the supply voltage continues to shrink in advanced nanometer technology nodes, motivating the exploration of alternative current mirror topologies.

#### B. Source Degenerated Current Mirror

As shown in Fig. 4(a), the transconductance of a transistor can be effectively decreased by placing a degeneration resistor in series with the source terminal. The effective transconductance  $G_m$  and the corresponding output noise are expressed

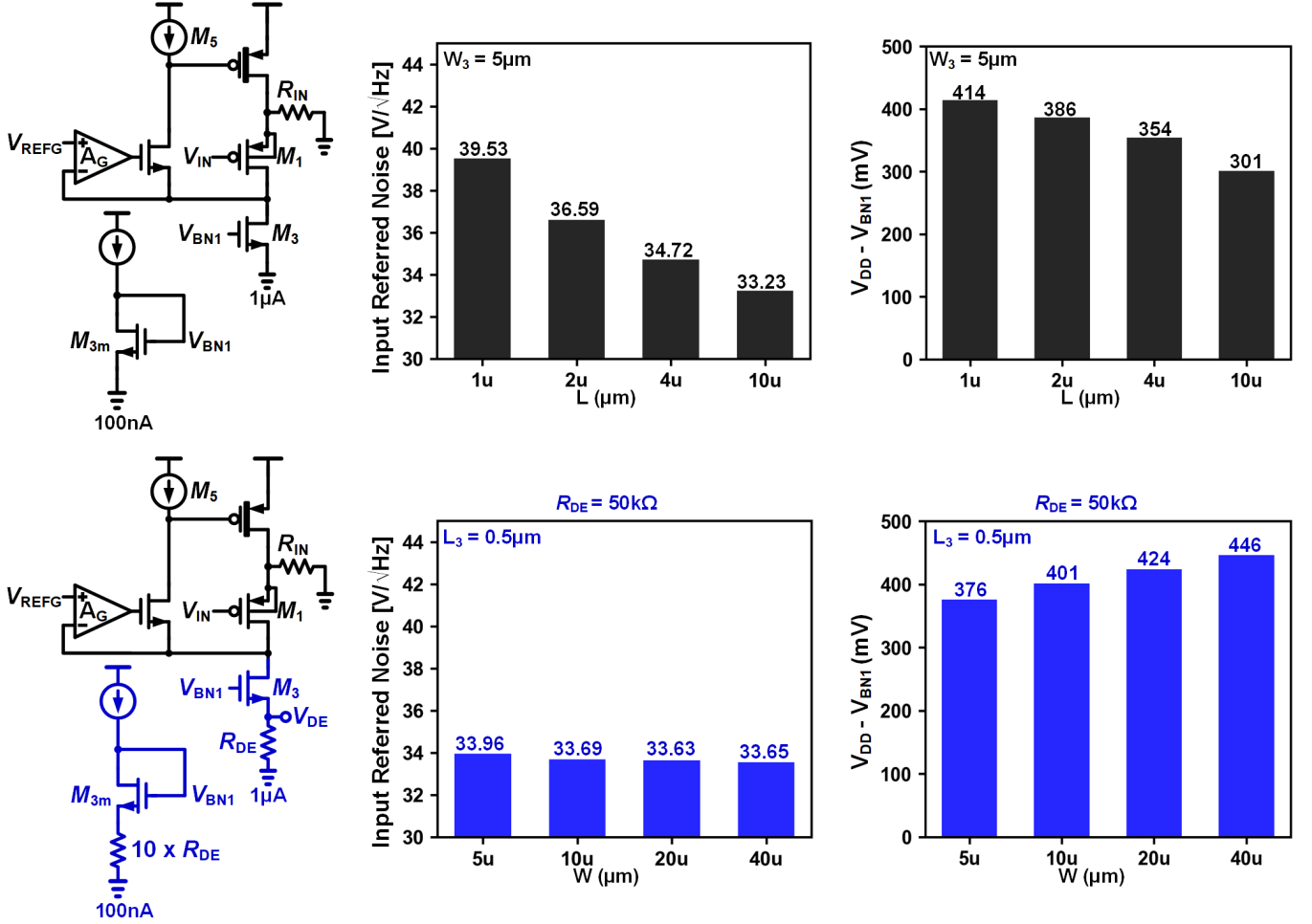


Fig. 5. Differential-mode half-circuit implementation and simulated performance comparison of current mirrors in the IA. The black bar plots represent the input-referred noise and voltage headroom versus transistor length  $L_3$  using a conventional current mirror, while the blue bar plots represent the input-referred noise and voltage headroom versus width  $W_3$  with a fixed  $R_{DE} = 50 \text{ k}\Omega$  using the proposed SDCM.

below, where the approximation holds under the condition  $g_{m3}R_{DE} \gg 1$ .

$$G_{m,M3} = \frac{\partial I_D}{\partial V_{G3}} = \frac{1}{1/g_{m3} + R_{DE}} \approx \frac{1}{R_{DE}} \quad (4)$$

$$\begin{aligned} \overline{v_{n,SDCM}^2} &= \left( \frac{i_{M3}^2 + (g_{m3}R_{DE})^2 i_{DE}^2}{(1 + g_{m3}R_{DE})^2} \right) R_D^2 + \overline{v_{RD}^2} \\ &= \left( \frac{4kT\gamma g_{m3} + (g_{m3}R_{DE})^2 4kT/R_{DE}}{(1 + g_{m3}R_{DE})^2} \right) R_D^2 \\ &\quad + \overline{v_{RD}^2} \\ &\approx \frac{4kT}{R_{DE}} \left( \frac{\gamma}{g_{m3}R_{DE}} + 1 \right) R_D^2 + \overline{v_{RD}^2} \end{aligned} \quad (5)$$

The complete derivation of Eq. (5) is provided in the Appendix. Eq. (4) shows that adding a degeneration resistor can directly reduce the effective transconductance of  $M_3$ , which is  $G_{m,M3}$ . Eq. (5) indicates that the noise contribution of  $M_3$ , which is  $i_{M3}^2 = 4kT\gamma g_{m3}$ , can be reduced by a factor of  $(1 + g_{m3}R_{DE})^2$  with an additional noise source from  $R_{DE}$ ,  $i_{DE}^2 = 4kT/R_{DE}$ . This reduction by the source degeneration comes from a local negative feedback similar to the

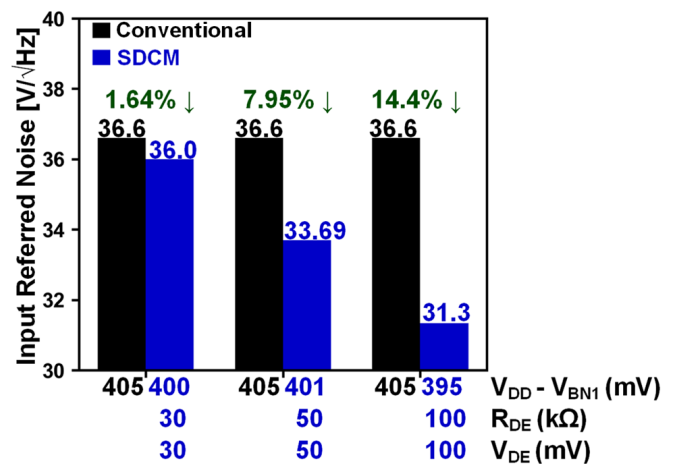


Fig. 6. Comparison of the input referred noise performance between conventional current mirror and SDCM, under the same voltage headroom near half- $V_{DD}$ .

source follower [21], reducing the effective transconductance  $G_{m3} = g_{m3}/(1 + g_{m3}R_{DE})$ , thereby leading to a decreased output noise.

As shown in Fig. 4(b) and (c), the SDCM achieves noise

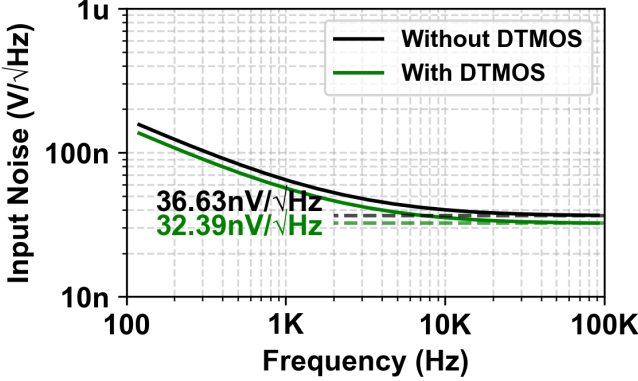


Fig. 7. Input referred noise performance with/without the DTMOS scheme.

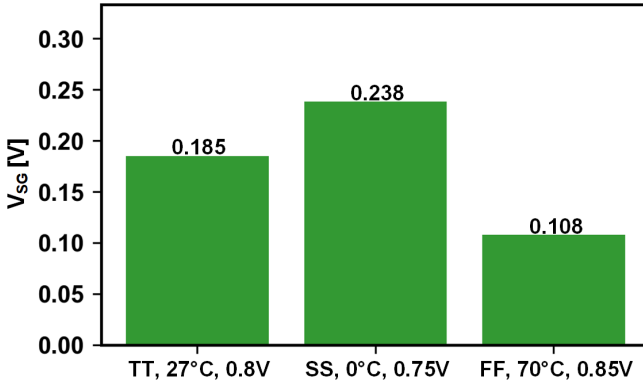


Fig. 8.  $V_{SG}$  of  $M_1$  across PVT in the DTMOS scheme.

reduction by increasing  $R_{DE}$ . However, a large  $R_{DE}$  not only suppresses output noise but also elevates the source nodes of the transistors as well, leading to a degraded voltage headroom which is a similar problem of the conventional current mirror. Since excessively large  $R_{DE}$  may drive  $M_3$  out of saturation and into the linear region,  $R_{DE}$  cannot be arbitrarily increased and must be carefully optimized.

Notably, Eq. (2) indicates that  $V_{GS}$  is inversely proportional to the transistor width for a fixed  $I_D$ . This property can be exploited as a design strategy to lower the diode-connected voltage  $V_{DIO}$  at  $M_{3m}$  and thereby recover the degraded headroom. As shown in Fig. 4(d), (e), increasing the width has a negligible impact on thermal noise, demonstrating that a larger width is an effective strategy to recover voltage headroom on the  $M_{3m}$  side from 450 mV to 610 mV without compromising noise performance. This is possible because Eq. (5) shows that the output noise PSD of the SDCM is no longer proportional to  $g_{m3}$ , unlike the conventional current mirror described in Eq. (3). In addition, the larger active area of the wider transistor in the SDCM helps reduce flicker noise. However, the additional voltage penalty  $V_{DE}$  introduced by the degeneration resistor  $R_{DE}$  on the mirrored side  $M_3$  remains unchanged regardless of transistor size, revealing a trade-off relationship between noise and headroom. Therefore, the designer must carefully optimize the transistor width and  $R_{DE}$  to achieve both low output noise and sufficient voltage headroom without significantly consuming the available voltage budget on the mirrored side.

By comparing Fig. 3(b), (c) with Fig. 4(d), (e), it can be

observed that when both the conventional current mirror and SDCM achieve a similar output noise level of approximately 230 nV/ $\sqrt{\text{Hz}}$ , the SDCM configured with a 100 k $\Omega$  of  $R_{DE}$  and a 20  $\mu\text{m}$  wide device width provides an additional 300 mV of voltage headroom compared to the conventional current mirror. However, this improvement comes at the cost of an extra voltage penalty of approximately 100 mV introduced by  $V_{DE}$  on the mirrored side due to the degeneration resistor  $R_{DE}$ .

### C. Integration and Performance Comparison in IA

To evaluate the practical impact of current mirror implementations within the IA, we developed two versions of IA, employing the conventional current mirror and the SDCM integrated into the TC stage. Fig. 5 illustrates both versions of the TC stage where differential mode half-circuit equivalents are drawn for simplicity, but the actual circuits are implemented in a differential architecture (see Fig. 9). We swept the length of the conventional current mirror in the first version and the width of the SDCM in the second version.

Note that although the SDCM approach has been widely used for noise reduction in current mirrors [22]–[24], limited discussions have been conducted in prior research on optimizing both noise reduction and voltage headroom. Our work aims to address the lack of discussions on the trade-off between noise and voltage headroom of the SDCM, when it is deployed in the TC stage of the IA.

As shown in Fig. 5, when both versions of the IA achieve a similar noise level approximately 33 nV/ $\sqrt{\text{Hz}}$ , the design with SDCM improves the voltage headroom at the  $M_{3m}$  branch by 145 mV when  $R_{DE} = 50$  k $\Omega$  was used. Fig. 6 shows another comparison in which  $R_{DE}$  is swept while ensuring a half  $V_{DD}$  of voltage headroom at the  $M_{3m}$  branch,  $V_{DD} - V_{BNI} \approx 400$  mV for a fair comparison, by optimizing the transistor dimensions. Under this condition, the SDCM achieves lower noise performance for larger  $R_{DE}$  values, reducing the input referred noise from 1.64% to 14.4% when  $R_{DE}$  increases from 30 k $\Omega$  to 100 k $\Omega$ . However, this benefit comes with an increase in the voltage drop  $R_{DE}$  in the main signal path of the TC stage, from 30 mV at  $R_{DE} = 30$  k $\Omega$  to 100 mV at  $R_{DE} = 100$  k $\Omega$ .

In this work, we adopted  $R_{DE} = 50$  k $\Omega$  in the design of IA considering a negligible  $V_{DE} = 50$  mV penalty at the TC stage but a 145 mV improved voltage headroom at the  $M_{3m}$  branch, achieving a 7.95% higher noise efficiency under the same power consumption.

### III. DYNAMIC THRESHOLD MOS

In conventional CMOS amplifier designs, the bulk terminal is typically connected to the source to eliminate the body effect by forcing  $V_{SB} = 0$ , to stabilize the variation of the threshold voltage  $V_{TH}$ . However, this configuration removes the bulk transconductance  $g_{mb}$  and thus does not fully utilize the opportunity to exploit the potential knob to maximize the  $g_m$  of the input transistor.

In this work, we connect the bulk terminal of the input transistor  $M_1$  to its gate as shown in Fig. 9, forming a DTMOS [25]. This technique introduces a positive  $V_{SB}$  equal

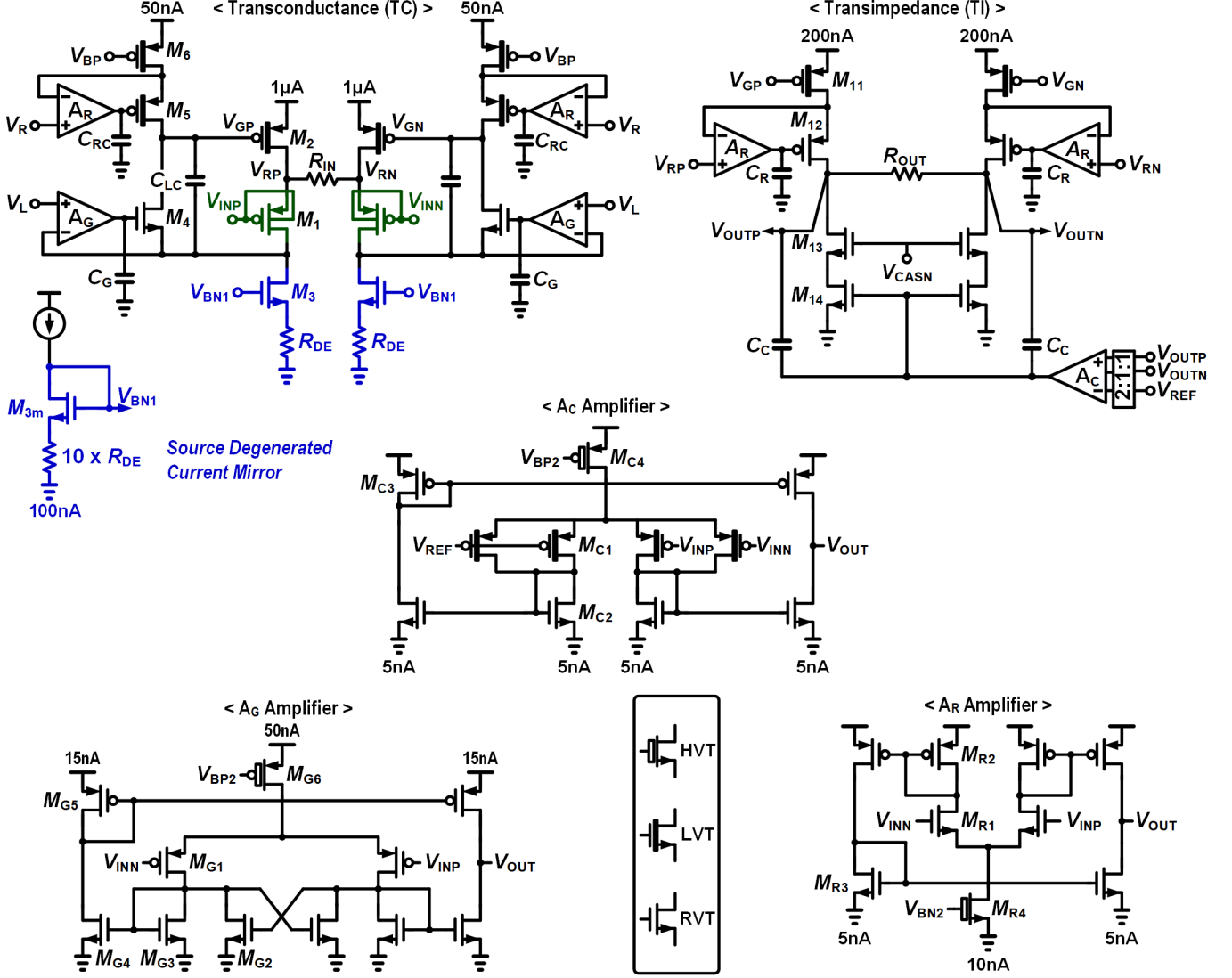


Fig. 9. Schematic of the proposed IA.

to the source-gate voltage  $V_{SG}$ , which dynamically modulates the threshold voltage  $V_{TH}$  and enhances the overall transconductance through body effect. The governing equations are as follows.

$$V_{TH} = V_{TH0} + \lambda \left( \sqrt{2\Phi_F + V_{SB}} - \sqrt{2\Phi_F} \right) \quad (6)$$

$$g_{mb} = \frac{\partial I_D}{\partial V_{BS}} = \mu_n C_{ox} \frac{W}{L} (V_{GS} - V_{TH}) \left( -\frac{\partial V_{TH}}{\partial V_{BS}} \right) \quad (7)$$

$$\frac{\partial V_{TH}}{\partial V_{BS}} = -\frac{\partial V_{TH}}{\partial V_{SB}} = -\frac{\lambda}{2} (2\Phi_F + V_{SB})^{-1/2} \quad (8)$$

$$g_{mb} = \frac{\partial I_D}{\partial V_{SB}} = g_m \frac{\lambda}{2\sqrt{2\Phi_F + V_{SB}}} \quad (9)$$

where  $\lambda$  denotes the body-effect coefficient and  $2\Phi_F$  is the inversion layer potential. Since the transconductance  $g_m$  of  $M_1$ , as indicated by Eq. (1), is inversely proportional to the input referred noise, the additional body transconductance  $g_{mb}$  in Eq. (9) introduced by the DTMOS boosts the effective transconductance of  $M_1$  from  $g_{m1}$  to  $g_{m1} + g_{mb1}$

thereby improving the noise performance. Fig. 7 compares the noise performance of the IA when the TC stage employs the DTMOS scheme over the baseline case. By dynamically enhancing effective transconductance through additional  $g_{mb}$ , the DTMOS configuration achieves a remarkable reduction in thermal noise. At 100 kHz, the input referred noise decreases from 36.63 nV/ $\sqrt{\text{Hz}}$  to 32.39 nV/ $\sqrt{\text{Hz}}$ , corresponding to an improvement of approximately 11.5%. Note that this noise benefit is achieved without increasing power consumption, as the DTMOS leverages body effect rather than higher bias currents to enhance the effective transconductance.

However, a potential issue of the DTMOS technique is the risk of forward biasing of the source-body junction. Since the bulk terminal is connected to the gate, a large positive  $V_{SB}$  may forward bias the source-body junction and activate the  $pn$  diode, which can lead to excessive leakage current or even transistor malfunction. Therefore, the maximum allowable  $V_{SG}$  must be carefully constrained to avoid forward conduction while maintaining the intended noise advantage.

To validate the safe operating region of the proposed

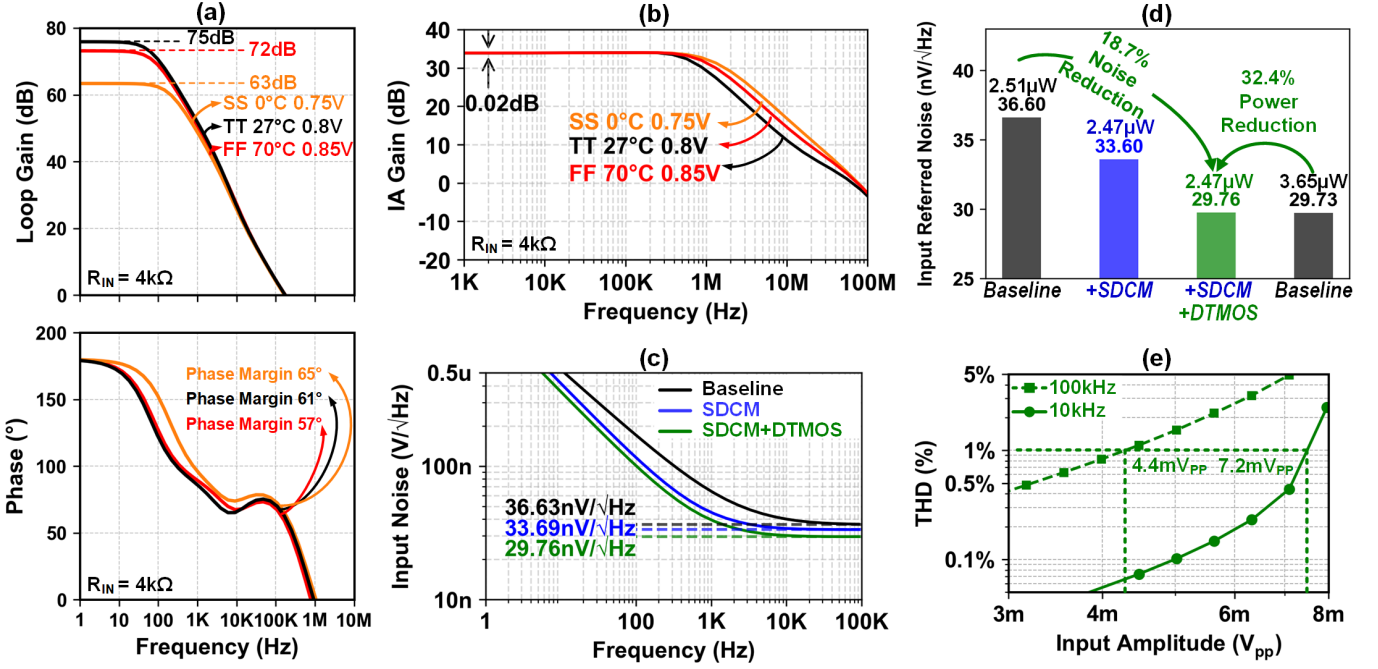


Fig. 10. Simulated (a) differential mode loop response of the FVF, (b) overall gain of the IA, (c) input referred noise, and (d) noise comparison. In (d),  $V_{DD} - V_{BN1}$  in Fig. 9, are 405 mV, 408 mV, 408 mV, 387 mV from the leftmost to rightmost bar, respectively, and (e) total harmonic distortion (THD) performance versus input amplitude at 10 kHz and 100 kHz.

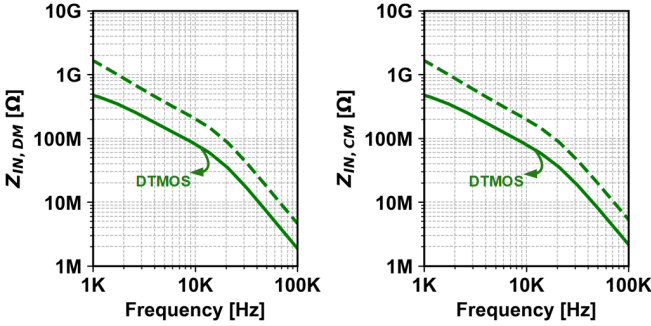


Fig. 11. Input impedance of the IA with/without the DTMOS scheme.

DTMOS configuration, a comprehensive PVT analysis was performed on the input PMOS  $M_1$ , as illustrated in Fig. 8. With the body and gate shorted,  $V_{SB}$  is equal to  $V_{SG}$ , and thus analyzing  $V_{SG}$  allows us to directly determine the forward-biasing condition of the body diode. Since the input transistor  $M_1$  is typically optimized to operate in the subthreshold region to maximize  $g_m$ ,  $V_{SG}$  could be kept lower than or close to  $V_{TH}$ . In our design, the worst-case simulated  $V_{SG}$  values are 185 mV, 238 mV, and 108 mV, all comfortably below 250 mV. Since parasitic diodes cannot be activated with such a negligible amount of forward bias [26], it is confirmed that the proposed DTMOS structure operates safely under the PVT corners while preserving the intended  $g_m$  benefits.

#### IV. SIMULATION RESULTS

Fig. 9 shows the complete transistor-level schematic of the proposed IA using the 28 nm CMOS process, which incorporates the SDCM and the DTMOS schemes into the

TC stage for low-noise, low-power operation. The detailed device parameters are summarized in Table II. A similar design strategy, as used in prior works [9], [10], was adopted to optimize the TC stage, including a sufficiently large width in  $M_1$  and assigning most of the current to the main branch ( $1 \mu\text{A}$ ), to maximize  $g_{m1}$  thereby suppressing input referred noise (see Eq. (1)). The lead compensation scheme ( $C_{LC}$ ) [9] was adopted for a power-bandwidth-efficient loop stabilization. We increased the width of the  $M_2$  transistor in TC stage to reduce its  $V_{SG}$  drop, to keep the voltage level of the  $V_{GP}$  node high. As such, a sufficient amount of voltage headroom could be given to the  $M_4$  transistor, resulting in the proper operation of the IA across PVT corners (see Fig. 10). Two auxiliary amplifiers in the TC stage and one in the TI stage were used for proper biasing: the drain regulation amplifier  $A_R$ , the gain-boosting amplifier  $A_G$ , and the common-mode feedback amplifier  $A_C$  [9], [10] where each current consumption was kept minimized to boost power efficiency. Within the TC stage,  $A_R$  not only ensures a proper distribution of  $V_{DS}$  of  $M_5$  and  $M_6$  but also acts as a gain-boosting amplifier, effectively increasing the output impedance and improving current mirroring accuracy. The  $A_G$  amplifier employs a positive feedback topology to significantly enhance its effective gain [10]. In the TI stage, an additional drain-regulation loop based on  $A_R$  is deployed to maintain accurate current mirroring from the TC stage. The  $A_C$  amplifier operates as a common-mode feedback circuit in the TI stage, continuously monitoring  $V_{OUTP}$  and  $V_{OUTN}$  to maintain a stable DC bias point.

Fig. 10 presents the key simulation results of the proposed IA, including the FVF loop response, input-referred noise, overall gain, and a comparative noise and power analysis with and without the proposed techniques. Using a gain-boosted

cascode current source ( $M_5$ ,  $M_6$ , and  $A_R$ ) together with a gain-boosted common-gate amplifier ( $M_4$  and  $A_G$ ), the IA achieves 75 dB differential-mode DC loop gain in the FVF loop even with a small  $R_{IN}$  of 4 k $\Omega$ . This high loop gain is maintained across process voltage temperature (PVT) corners. As a result, Fig. 10(b) shows a robust 34 dB closed-loop AC gain across PVT corners, with less than 0.02 dB variation, while the nominal case achieves a bandwidth of 1.44 MHz. As illustrated in Fig. 10(c), applying the SDCM and DTMOS techniques reduces the input-referred noise from 36.63 nV/ $\sqrt{\text{Hz}}$  in the baseline design to 33.69 nV/ $\sqrt{\text{Hz}}$  and 29.76 nV/ $\sqrt{\text{Hz}}$ , corresponding to 7.95% and 11.7% reductions, achieving an overall improvement of 18.7%. Fig. 10(d) compares the baseline and proposed IA under the same  $V_{DD} - V_{BN1}$  biasing condition, showing that the proposed design achieves equivalent noise performance while consuming 32.4% less power compared to the baseline IA under iso-noise condition, demonstrating superior noise efficiency. This amount of power reduction makes a good agreement with the theoretical estimation, i.e.,  $(1 - 0.187)^2 = 1 - 0.339$ , corresponding to a 33.9% reduction that is close to our result of 32.4%. This agreement follows from the fact that the input referred RMS noise of low-power amplifiers is inversely proportional to the square root of the current, e.g., the noise efficiency factor (NEF) [27], [28]. Fig. 10(e) illustrates THD performance (up to 10<sup>th</sup> harmonic) at both 10 kHz and 100 kHz using the PSS simulation in the Spectre environment, confirming that the circuit maintains 1% THD with 7.2 mV<sub>PP</sub> and 4.4 mV<sub>PP</sub> input amplitudes, respectively.

While the proposed DTMOS technique effectively improves transconductance and reduces input-referred noise, it introduces a trade-off in the input impedance characteristics. As shown in Fig. 11, connecting the bulk terminal to the gate effectively adds an additional parasitic capacitance at the input node, which lowers both the differential-mode and common-mode input impedances across the entire frequency range. Although the achieved input impedance remains sufficient ( $\approx 7 \text{ M}\Omega$  at 50 kHz) for most wet type, four-electrode BioZ sensing scenarios, where its typical value ranges from 500  $\Omega$ -2 k $\Omega$  depending on measurement frequency and contact status [29], this reduction could affect signal integrity in ultra-high-impedance electrodes such as  $< 1 \text{ cm}^2$  dry type electrodes [13]. Future work may focus on optimizing the DTMOS scheme or introducing impedance boosting techniques [13], [30] to mitigate the adverse impact on the input impedance without compromising the noise benefit.

The simulated performance of the proposed IA is summarized in Table I and compared with other recent state-of-the-art IA designs. Our design with  $R_{IN} = 4 \text{ k}\Omega$  achieves a 21% lower power consumption, 26% lower input referred noise, 3.9x higher bandwidth than [10], while achieving a similar input linear range even under the 20% lower supply voltage. Compared to [2], [31], our design with  $R_{IN} = 20 \text{ k}\Omega$  achieves superior noise and bandwidth performance while maintaining a comparable input range. Notably, this input range is obtained even at a supply voltage of 0.8 V despite the reduced headroom, which is significantly lower than 1.8 V used in [2], [31].

## V. CONCLUSION

We have presented a low-power, low-noise IA for BioZ sensing applications, which exploits SDCM and DTMOS techniques. Simulated in a 28 nm CMOS process, it consumes 2.5  $\mu\text{W}$  power dissipation with a power supply of 0.8 V, while demonstrating an input-referred noise of 30 nV/ $\sqrt{\text{Hz}}$  within a 1.44 MHz bandwidth at  $R_{IN} = 4 \text{ k}\Omega$  and  $R_{DE} = 50 \text{ k}\Omega$ . Discussions on the noise-headroom trade-off in SDCM, and the noise-input impedance trade-off in DTMOS are provided. By combining the SDCM and DTMOS techniques, the input-referred noise is reduced by 18.7%, which is translated to a 32.4% power saving under the same noise performance compared to the baseline design.

By providing a low-power, low-noise core amplifier structure for BioZ sensors, our design offers a fundamental building block that can be seamlessly integrated into advanced voltage readout techniques recently published in the literature, such as baseline cancellation [14], [29], differential difference amplifiers [1], and  $\Delta\Sigma$  modulators [14]. The complete design parameters have been open-sourced to promote reproducibility and support future research developments.

## APPENDIX

This appendix presents the derivation of the output-referred noise in the source-degenerated current mirror (SDCM), as described in Eq. (5).

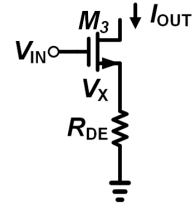


Fig. 12. Common-source stage with source degeneration.

The output noise current consists of two primary contributions: 1) the thermal noise of the degeneration resistor  $R_{DE}$ , and 2) the thermal noise of the mirroring transistor  $M_3$ . In this analysis, we use the superposition principle of the noise PSD after calculating each noise contribution, since two noise sources are uncorrelated. Note that noise currents cause small-signal voltage fluctuations  $v_x$  that force the transistor to behave as a conductor, injecting a small signal current  $g_{m3}v_{gs3}$  back into the  $v_x$  node, thereby creating feedback. Due to this local negative feedback introduced by  $R_{DE}$  [21], the impact of the noise coming from the mirroring transistor  $M_3$  is attenuated by a factor related to the loop gain  $g_{m3}R_{DE}$ , similar to the case of noise contribution of cascode devices (see Chapter 7.4.4 in [19]).

First, let us analyze the thermal noise current generated by  $R_{DE}$ . We use the correlated decomposition model of current noise (see Chapter 7.6 in [19]). As shown in Fig. 13, the noise current can be decomposed into two correlated current sources where the noise current connected to GND in both terminals can be omitted since its noise current flows directly to GND, leaving the circuit unaffected. The resulting noise

TABLE I  
PERFORMANCE COMPARISON TABLE - LOW-POWER IA ( $<10 \mu\text{W}$ ) for BioZ Sensors

| Low-Power IA                    | TBioCAS'13 [31] | ESSCIRC'17 [2] | JSSC'20 [9]  | TBioCAS'22 [32]  | ISCAS'23 [10] | This Work ( $R_{\text{IN}} = 4 \text{k}\Omega$ ) | This Work ( $R_{\text{IN}} = 20 \text{k}\Omega$ ) |
|---------------------------------|-----------------|----------------|--------------|------------------|---------------|--|---|
| Process (nm)                    | 180             | 180            | 65           | 180              | 65            |  | <b>28</b>   |
| Supply (V)                      | 1.8             | 1.8            | 0.5          | 1.0              | 1.0           |  | <b>0.8</b>  |
| Gain (dB)                       | 30              | 36             | 31           | 51               | 40            | <b>34</b>  | <b>20</b>   |
| Power ( $\mu\text{W}$ )         | 2.16            | 2.12           | 3.95         | 0.7              | 3.11          |  | <b>2.47</b>                                       |
| Noise (nV/ $\sqrt{\text{Hz}}$ ) | 149             | 115            | 45           | 300 <sup>A</sup> | 40            | <b>29.76</b>                                     | <b>46.18</b>                                      |
| Bandwidth (Hz)                  | 20 k            | 20 k           | 408 k        | 3 k              | 369 k         | <b>1.44 M</b>                                    | <b>4.67 M</b>                                     |
| Input Range (mV <sub>PP</sub> ) | 44 (20 kHz)     | 52 (20 kHz)    | 1.6 (20 kHz) | 10               | 7.26 (10 kHz) | <b>7.2 (10 kHz)</b>                              | <b>40 (10 kHz)</b>                                |
|                                 |                 |                |              |                  |               | <b>4.4 (100 kHz)</b>                             | <b>32 (100 kHz)</b>                               |

<sup>A</sup>Estimated from figure

TABLE II  
DESIGN PARAMETERS OF PROPOSED IA.

| TC stage         | W/L ( $\mu\text{m}$ )         | $A_R$ Amplifier  | W/L ( $\mu\text{m}$ ) |
|------------------|-------------------------------|------------------|-----------------------|
| $M_1$            | 500/0.25                      | $M_{R1}$         | 0.25/1                |
| $M_2$            | 30/0.5                        | $M_{R2}$         | 1/1                   |
| $M_{3m}$         | 2/1                           | $M_{R3}$         | 0.25/0.25             |
| $M_3$            | 20/1                          | $M_{R4}$         | 0.25/1                |
| $M_4$            | 0.25/1                        | $C_{RC}$         | 10 fF                 |
| $M_5$            | 1/1                           | $A_G$ Amplifier  | W/L ( $\mu\text{m}$ ) |
| $M_6$            | 1/1                           |                  |                       |
| $V_R$            | 100 mV                        | $M_{G1}$         | 0.25/0.25             |
| $V_L$            | 250 mV                        | $M_{G2}$         | 0.8/1                 |
| $C_{LC}$         | 750 fF                        | $M_{G3}$         | 1/1                   |
| $R_{DE}$         | 50 k $\Omega$                 | $M_{G4}$         | 1/1                   |
| $R_{IN}$         | 4 k $\Omega$ or 20 k $\Omega$ | $M_{G5}$         | 0.25/0.25             |
|                  |                               | $M_{G6}$         | 0.3/1                 |
|                  |                               | $C_G$            | 5 pF                  |
| TI stage         | W/L ( $\mu\text{m}$ )         | $A_C$ Amplifier  | W/L ( $\mu\text{m}$ ) |
| $M_{11}$         | 6/0.5                         | $M_{C1}$         | 1/1                   |
| $M_{12}$         | 1/0.25                        | $M_{C2}$         | 0.25/0.25             |
| $M_{13}$         | 0.5/0.5                       | $M_{C3}$         | 0.25/0.25             |
| $M_{14}$         | 0.25/4                        | $M_{C4}$         | 0.25/1                |
| $C_C$            | 5 fF                          | $V_{\text{REF}}$ | 400 mV                |
| $C_R$            | 20 fF                         |                  |                       |
| $R_{\text{OUT}}$ | $250 \times R_{\text{IN}}$    |                  |                       |

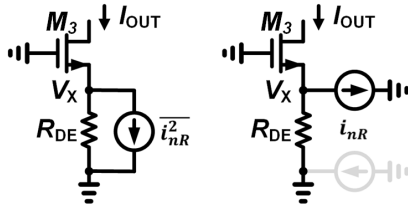


Fig. 13. Current noise model for resistor  $R_{\text{DE}}$  in the feedback loop.

current contributed by  $R_{\text{DE}}$ , e.g.,  $i_{n,\text{out}}|_{R_{\text{DE}}}$ , on the drain side of the transistor can be expressed as the following, when we neglect channel-length modulation:

$$i_{n,\text{out}}|_{R_{\text{DE}}} = \frac{v_x}{R_{\text{DE}}} + i_{nR}. \quad (10)$$

Since this current must be equal to the small-signal current from the transistor:

$$i_{n,\text{out}}|_{R_{\text{DE}}} = -g_{m3}v_x. \quad (11)$$

Solving for  $v_x$  gives:

$$v_x = -\frac{R_{\text{DE}}}{1 + g_{m3}R_{\text{DE}}}i_{nR}, \quad (12)$$

which leads to:

$$i_{n,\text{out}}|_{R_{\text{DE}}} = \frac{g_{m3}R_{\text{DE}}}{1 + g_{m3}R_{\text{DE}}}i_{nR}. \quad (13)$$

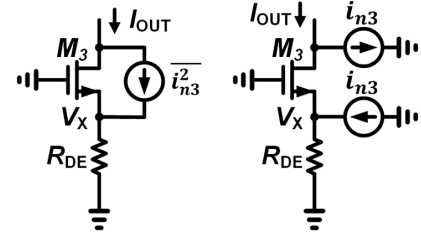


Fig. 14. Current noise model for  $M_3$  in the feedback loop.

Now, consider the noise contributed by  $M_3$ , e.g.,  $i_{n,\text{out}}|_{M_3}$ , as shown in Fig. 14:

$$i_{n,\text{out}}|_{M_3} = \frac{v_x}{R_{\text{DE}}} = -g_{m3}v_x + i_{n3}. \quad (14)$$

Solving again gives:

$$v_x = \frac{R_{\text{DE}}}{1 + g_{m3}R_{\text{DE}}}i_{n3}, \quad (15)$$

and:

$$i_{n,\text{out}}|_{M_3} = \frac{1}{1 + g_{m3}R_{\text{DE}}}i_{n3}. \quad (16)$$

Combining both components in the power domain, the total output current noise becomes:

$$\begin{aligned} \overline{i_{n,\text{out}}^2} &= \overline{i_{n,\text{out}}^2|_{R_{\text{DE}}}} + \overline{i_{n,\text{out}}^2|_{M_3}} \\ &= \left( \frac{g_{m3}R_{\text{DE}}}{1 + g_{m3}R_{\text{DE}}} \right)^2 \overline{i_{nR}^2} + \left( \frac{1}{1 + g_{m3}R_{\text{DE}}} \right)^2 \overline{i_{n3}^2}. \end{aligned} \quad (17)$$

Substituting the following:

$$\overline{i_{nR}^2} = \frac{4kT}{R_{\text{DE}}}, \quad \overline{i_{n3}^2} = 4kT\gamma g_{m3},$$

we obtain the total output voltage noise of SDCM shown in Fig. 4 and Eq. (5):

$$\begin{aligned} \overline{v_{n,\text{SDCM}}^2} &= \left( \frac{4kT\gamma g_{m3} + (g_{m3}R_{\text{DE}})^2 4kT/R_{\text{DE}}}{(1 + g_{m3}R_{\text{DE}})^2} \right) R_{\text{D}}^2 \\ &\quad + \overline{v_{RD}^2} \end{aligned} \quad (18)$$

## REFERENCES

[1] S.-I. Cheon, H. Choi, G. Yun, S. Oh, J.-H. Suh, S. Ha, and M. Je, "A Two-Electrode Bio-Impedance Readout IC with Complex-Domain Noise-Correlated Baseline Cancellation Supporting Sinusoidal Excitation," in *IEEE International Solid-State Circuits Conference (ISSCC)*, vol. 67, 2024, pp. 556–558.

[2] K. Kim, K. Song, K. Bong, J. Lee, K. Lee, Y. Lee, U. Ha, and H.-J. Yoo, "A 24  $\mu$ W 38.51 m $\Omega$ rms Resolution Bio-Impedance Sensor with Dual Path Instrumentation Amplifier," in *IEEE European Solid State Circuits Conference (ESSCIRC)*, 2017, pp. 223–226.

[3] S. Ollmar, A. Fernandez Schrunder, U. Birgersson, T. Kristoffersson, A. Rusu, E. Thorsson, P. Hedenqvist, E. Manell, A. Rydén, M. Jensen-Waern, and S. Rodriguez, "A battery-less implantable glucose sensor based on electrical impedance spectroscopy," *Scientific Reports*, vol. 13, no. 1, p. 18122, 2023.

[4] K. Song, U. Ha, S. Park, J. Bae, and H.-J. Yoo, "An Impedance and Multi-Wavelength Near-Infrared Spectroscopy IC for Non-Invasive Blood Glucose Estimation," *IEEE Journal of Solid-State Circuits (JSSC)*, vol. 50, no. 4, pp. 1025–1037, 2015.

[5] D. Jiang, Y. Wu, and A. Demosthenous, "Hand Gesture Recognition Using Three-Dimensional Electrical Impedance Tomography," *IEEE Transactions on Circuits and Systems II: Express Briefs*, vol. 67, no. 9, pp. 1554–1558, 2020.

[6] J. Lee, S. Gweon, K. Lee, S. Um, K.-R. Lee, K. Kim, J. Lee, and H.-J. Yoo, "A 9.6 mW/Ch 10 MHz Wide-bandwidth Electrical Impedance Tomography IC with Accurate Phase Compensation for Breast Cancer Detection," in *IEEE Custom Integrated Circuits Conference (CICC)*, 2020.

[7] Q. Pan, Q. Luo, T. Qu, L. Liu, X. Li, M. Chen, Z. Hong, and J. Xu, "A 97.3-dB SNR Bioimpedance AFE With -84-dB THD Segmented-  $\Delta\Sigma$  M Sinusoidal Current Generator and Passing-Through Instrumentation Amplifier," *IEEE Journal of Solid-State Circuits (JSSC)*, vol. 60, no. 4, pp. 1411–1422, 2025.

[8] M. Kim, J. Jang, H. Kim, J. Lee, J. Lee, K.-R. Lee, K. Kim, Y. Lee, K. J. Lee, and H.-J. Yoo, "A 1.4-m $\Omega$ -Sensitivity 94-dB Dynamic-Range Electrical Impedance Tomography SoC and 48-Channel Hub-SoC for 3-D Lung Ventilation Monitoring System," *IEEE Journal of Solid-State Circuits (JSSC)*, vol. 52, no. 11, pp. 2829–2842, Nov. 2017.

[9] K. Kim, J.-H. Kim, S. Gweon, M. Kim, and H.-J. Yoo, "A 0.5 V Sub-10  $\mu$ W 15.28 m $\Omega$ / $\sqrt{\text{Hz}}$  Bio-Impedance Sensor IC with Sub-1° Phase Error," *IEEE Journal of Solid-State Circuits (JSSC)*, vol. 55, no. 8, pp. 2161–2173, Aug. 2020.

[10] K. Kim and S.-C. Liu, "A 3.11  $\mu$ W 40 nV/ $\sqrt{\text{Hz}}$  Instrumentation Amplifier for Bio-Impedance Sensors Exploiting Positive-Feedback-Assisted Gain Boosting," *IEEE International Symposium on Circuits and Systems (ISCAS)*, pp. 1–5, July . 2023.

[11] Y.-C. Teng and K. M. Odame, "A 10 MHz 85 dB dynamic range instrumentation amplifier for electrical impedance tomography," in *IEEE Biomedical Circuits and Systems Conference (BioCAS)*, 2014, pp. 632–635.

[12] M. Takhti and K. Odame, "A Power Adaptive, 1.22-pW/Hz, 10-MHz Read-Out Front-End for Bio-Impedance Measurement," *IEEE Transactions on Biomedical Circuits and Systems (TBioCAS)*, vol. 13, no. 4, pp. 725–734, 2019.

[13] Q. Pan, T. Qu, B. Tang, F. Shan, Z. Hong, and J. Xu, "A 0.5-m $\Omega$ / $\sqrt{\text{Hz}}$  Dry-Electrode Bioimpedance Interface With Current Mismatch Cancellation and Input Impedance of 100 M $\Omega$  at 50 kHz," *IEEE Journal of Solid-State Circuits (JSSC)*, vol. 58, no. 6, pp. 1735–1745, 2023.

[14] T.-T. Zhang, H. Son, J. Zhao, C.-H. Heng, and Y. Gao, "A 26.6–119.3- $\mu$ W 101.9-dB SNR Direct Digitization Bio-Impedance Readout IC," *IEEE Journal of Solid-State Circuits (JSSC)*, vol. 58, no. 9, pp. 2619–2631, 2023.

[15] B. Nauta, "Racing Down the Slopes of Moore's Law," in *IEEE International Solid-State Circuits Conference (ISSCC)*, vol. 67, 2024, pp. 16–23.

[16] P. Kinget, "Short Course: Designing Ultra Low Voltage Analog and Mixed Signal Circuits," in *IEEE International Solid-State Circuits Conference (ISSCC) Digest of Technical Papers*, vol. TUTORIAL, 2015, pp. 1–29.

[17] K. Kim, C. Gao, R. Graça, I. Kiselev, H.-J. Yoo, T. Delbruck, and S.-C. Liu, "A 23- $\mu$ W Keyword Spotting IC With Ring-Oscillator-Based Time-Domain Feature Extraction," *IEEE Journal of Solid-State Circuits (JSSC)*, vol. 57, no. 11, pp. 3298–3311, 2022.

[18] Y. Xue and K. Kim, "A 2.48  $\mu$ W 33.13 nV/ $\sqrt{\text{Hz}}$  Instrumentation Amplifier for Bio-Impedance Sensors with Source Degenerated Current Mirror and DTMOS Transistor," in *2025 23rd IEEE Interregional NEWCAS Conference (NEWCAS)*, 2025, pp. 371–375.

[19] B. Razavi, *Design of Analog CMOS Integrated Circuits*, 2nd ed. McGraw-Hill, 2017, Chapter 7.4.2: Common-Gate Stage.

[20] A. Arnaud, R. Fiorelli, and C. Galup-Montoro, "Nanowatt, Sub-nS OTAs, With Sub-10-mV Input Offset, Using Series-Parallel Current Mirrors," *IEEE Journal of Solid-State Circuits (JSSC)*, vol. 41, no. 9, pp. 2009–2018, 2006.

[21] K. Kim and S.-C. Liu, "Continuous-Time Analog Filters for Audio Edge Intelligence: Review on Circuit Designs," *IEEE Circuits and Systems Magazine*, vol. 23, no. 2, pp. 29–48, 2023.

[22] W. Sansen, *Analog Design Essentials*. New York: Springer, 2006, Chapter 4: Noise performance of elementary transistor stages.

[23] X. Yang, M. Ballini, C. Sawigun, W.-Y. Hsu, J.-W. Weijers, J. Putzeys, and C. M. Lopez, "An AC-Coupled 1st-Order  $\Delta - \Delta\Sigma$  Readout IC for Area-Efficient Neural Signal Acquisition," *IEEE Journal of Solid-State Circuits*, vol. 58, no. 4, pp. 949–960, 2023.

[24] W. Choi, J. Angevare, I. Park, K. A. A. Makinwa, and Y. Chae, "A 0.9-V 28-MHz Highly Digital CMOS Dual-RC Frequency Reference With  $\pm 200$  ppm Inaccuracy From -40 °C to 85 °C," *IEEE Journal of Solid-State Circuits (JSSC)*, vol. 57, no. 8, pp. 2418–2428, 2022.

[25] F. Assaderaghi, D. Sinitsky, S. Parke, J. Bokor, P. Ko, and C. Hu, "Dynamic threshold-voltage MOSFET (DTMOS) for ultra-low voltage VLSI," *IEEE Transactions on Electron Devices*, vol. 44, no. 3, pp. 414–422, 1997.

[26] S. Chatterjee, Y. Tsividis, and P. Kinget, "0.5-V analog circuit techniques and their application in OTA and filter design," *IEEE Journal of Solid-State Circuits (JSSC)*, vol. 40, no. 12, pp. 2373–2387, 2005.

[27] M. Steyaert and W. Sansen, "A micropower low-noise monolithic instrumentation amplifier for medical purposes," *IEEE Journal of Solid-State Circuits (JSSC)*, vol. 22, no. 6, pp. 1163–1168, 1987.

[28] R. Harrison and C. Charles, "A low-power low-noise CMOS amplifier for neural recording applications," *IEEE Journal of Solid-State Circuits (JSSC)*, vol. 38, no. 6, pp. 958–965, 2003.

[29] H. Ha, W. Sijbers, R. Van Wegberg, J. Xu, M. Konijnenburg, P. Vis, A. Breeschoten, S. Song, C. Van Hoof, and N. V. Helleputte, "A Bio-Impedance Readout IC With Digital-Assisted Baseline Cancellation for Two-Electrode Measurement," *IEEE Journal of Solid-State Circuits (JSSC)*, vol. 54, no. 11, pp. 2969–2979, 2019.

[30] Y. Zhong, L. Jie, and N. Sun, "A 78.6 dB-SNDR 520mV<sub>pp</sub>-full-scale 620M $\Omega$ -Z<sub>in</sub> 105dB-CMRR VCO-based Sensor Readout Circuit Using FVF-Based Gm-Input Structure," in *IEEE Asian Solid-State Circuits Conference (A-SSCC)*, 2022, pp. 1–3.

[31] L. Yan, J. Pettine, S. Mitra, S. Kim, D.-W. Jee, H. Kim, M. Osawa, Y. Harada, K. Tamiya, C. Van Hoof, and R. F. Yazicioglu, "A 13  $\mu$ A Analog Signal Processing IC for Accurate Recognition of Multiple Intra-Cardiac Signals," *IEEE Transactions on Biomedical Circuits and Systems (TBioCAS)*, vol. 7, no. 6, pp. 785–795, 2013.

[32] H. Rezaee-Dehsorkh, N. Ravanshad, A. Shamsaki, M. R. Fakour, and P. Aliparast, "A Low-Power Single-Path Bio-Impedance Measurement System Using an Analog-to-Digital Converter for I/Q Demodulation," *IEEE Transactions on Biomedical Circuits and Systems (TBioCAS)*, 2022.



**Yu Xue** (Student Member, IEEE) received the B.S. degree in electronic information engineering from Nanjing Tech University, Nanjing, China, in 2022. He is currently pursuing the M.S. degree in electronics and nanotechnology at Aalto University, Espoo, Finland, where he is working with the Tiny Systems and Circuits (TSirc) Research Group. His current research interests include low-noise and low-power instrumentation amplifiers for biomedical sensing applications.



**Kwantae Kim** (Senior Member, IEEE) received B.S., M.S., and Ph.D. degrees in the School of Electrical Engineering, KAIST, South Korea, in 2015, 2017, and 2021, respectively. He is an Assistant Professor at the Department of Electronics and Nanoengineering, School of Electrical Engineering, Aalto University, Finland. He was a Visiting Student in 2020, and a Postdoctoral Researcher from 2021 to 2023, at the Institute of Neuroinformatics, University of Zurich and ETH Zurich, and an Established Researcher from 2023 to 2024, at the Department of Information Technology and Electrical Engineering, ETH Zurich, Switzerland. His research interests include analog/mixed-signal ICs and full-custom memory ICs for neuromorphic signal processing, biomedical sensors, and flexible electronics.

Information Technology and Electrical Engineering, ETH Zurich, Switzerland. His research interests include analog/mixed-signal ICs and full-custom memory ICs for neuromorphic signal processing, biomedical sensors, and flexible electronics.